Applied Surface Science 541 (2021) 148612

Contents lists available at ScienceDirect

Applied Surface Science

journal homepage: www.elsevier.com/locate/apsusc

Full Length Article

Magnesium-intercalated graphene on SiC: Highly n-doped air-stable bilayer graphene at extreme displacement fields

Antonija Grubišić-Čabo [a,*,1], Jimmy C. Kotsakidis [a], Yuefeng Yin [b,c], Anton Tadich [c,d,e], Matthew Haldon [a], Sean Solari [a], Iolanda Di Bernardo [a,c], Kevin M. Daniels [f], John Riley [e], Eric Huwald [e], Mark T. Edmonds [a,c], Rachael Myers-Ward [g], Nikhil V. Medhekar [b,c], D. Kurt Gaskill [h], Michael S. Fuhrer [a,c,*]

[a] School of Physics and Astronomy, Monash University, Clayton, VIC 3800, Australia
[b] Department of Materials Science and Engineering, Monash University, Clayton, VIC 3800, Australia
[c] Centre for Future Low Energy Electronics Technologies, Monash University, Clayton, VIC 3800, Australia
[d] Australian Synchrotron, Clayton, VIC 3168, Australia
[e] Department of Physics, La Trobe University, Bundoora, VIC 3086, Australia
[f] Department of ECE, University of Maryland, College Park, MD 20742, USA
[g] U.S. Naval Research Laboratory, Washington D.C. 20375, USA
[h] Institute for Research in Electronics and Applied Physics, University of Maryland, College Park, MD 20742, United States

ARTICLE INFO

Keywords:
Graphene
Extremely high displacement field
Electronic structure
ARPES
Air exposure

ABSTRACT

We use angle-resolved photoemission spectroscopy to investigate the electronic structure of bilayer graphene at high n-doping and extreme displacement fields, created by intercalating epitaxial monolayer graphene on silicon carbide with magnesium to form quasi-freestanding bilayer graphene on magnesium-terminated silicon carbide. Angle-resolved photoemission spectroscopy reveals that upon magnesium intercalation, the single massless Dirac band of epitaxial monolayer graphene is transformed into the characteristic massive double-band Dirac spectrum of quasi-freestanding bilayer graphene. Analysis of the spectrum using a simple tight binding model indicates that magnesium intercalation results in an n-type doping of 2.1×10^{14} cm^{-2} and creates an extremely high displacement field of 2.6 V/nm, thus opening a considerable gap of 0.36 eV at the Dirac point. This is further confirmed by density-functional theory calculations for quasi-freestanding bilayer graphene on magnesium-terminated silicon carbide, which show a similar doping level, displacement field and bandgap. Finally, magnesium-intercalated samples are surprisingly robust to ambient conditions; no significant changes in the electronic structure are observed after 30 min exposure to air.

1. Introduction

Graphene, a single layer of sp^2 bonded carbon atoms [1], has an exceptionally high intrinsic electrical conductivity [2], yet is nearly 98% transparent to light [3] across a broad spectrum of wavelengths, making it attractive as a transparent conductor for a variety of applications.

Moreover, doping may be used to significantly modify graphene's electrical and optical properties. Graphene's conductivity can be tuned dramatically with doping [1], and in highly-doped graphene achieved via chemical means [4,5] the conductivity can often reach values near the intrinsic limit set by room temperature acoustic phonon scattering. Doping can be used to alter graphene's workfunction [6], which can be exploited to make new types of electronic devices [7] or more efficient contacts to semiconductors [8]. Doping also alters graphene's optical

Abbreviations: EMLG, epitaxial monolayer graphene; ARPES, angle-resolved photoemission spectroscopy; SiC, silicon carbide; Mg-QFSBLG, quasi-freestanding bilayer graphene on magnesium terminated silicon carbide; LEED, low-energy electron diffraction; UHV, ultra-high vacuum; hυ, photon energy; E_{Bin}, binding energy; E_F, Fermi energy; θ, polar emission angle; φ, azimuthal angle; DFT, density-functional theory; VASP, Vienna ab initio Simulation Package; PBE, Perdew-Burke-Ernzhof; GGA, generalized gradient approximation; MDCs, momentum distribution curves.

* Corresponding authors at: School of Physics and Astronomy, Monash University, Clayton, VIC 3800, Australia (M.S. Fuhrer).
E-mail addresses: Antonija@kth.se (A. Grubišić-Čabo), Michael.Fuhrer@monash.edu (M.S. Fuhrer).
[1] KTH, Applied Physics, Stockholm SE 114 19, Sweden.

https://doi.org/10.1016/j.apsusc.2020.148612
Received 3 October 2020; Received in revised form 11 November 2020; Accepted 24 November 2020
Available online 28 November 2020

absorption properties. For example, Pauli blocking, where interband optical transitions for energies lower than twice the Fermi energy are forbidden, causes an increase in transparency, an effect which can be exploited for optoelectronic switching [9] or increased performance in transparent conductors [5,10]. In bilayer graphene [11,12], doping can produce a displacement field which opens a bandgap at the Dirac point, additionally altering the electronic and optical properties [13–19].

A variety of approaches have been used to tune graphene's properties via doping, including field-effect gating [6,20–23], electric double layer gating [17,24–27], electrolytic gating [28–31], chemical substitution [32–36], adsorption [13,37–43], and intercalation [42–44,48,51–57]. Among these, chemical doping offers a simple, powerful approach to create highly-doped graphene layers which can be incorporated as transparent conductors, electrodes or optical elements in a wide variety of device structures. To be widely applicable, the chemical doping approach should result in a highly-doped graphene layer which is stable under processing conditions such as ambient exposure and high temperature. Several chemical doping approaches have been demonstrated to successfully produce stable highly p-doped graphene [52,58–61] with p-type carrier densities exceeding 10^{14} cm^{-2}. Stable n-doped graphene is also desirable, particularly for applications requiring low work function (as compared to an increased work function in the case of p-doping). However, the production of stable n-doped graphene has been more difficult, with only a few demonstrations [46,62,63]. The difficulty in producing stable n-doped graphene is, in large part, due to the highly reactive and air-unstable nature of n-type dopants. Despite this, highly air-stable, n-doped single-layer graphene was obtained by $CsCO_3$ [62] and ZnO doping [63], attaining electron concentrations of 2.2×10^{13} cm^{-2} and $>5.76 \times 10^{12}$ cm^{-2}, respectively. These values do not significantly exceed the natural doping found in epitaxial monolayer graphene (EMLG) on silicon carbide [64], so achieving extremely high and stable n-doped graphene remains an open challenge.

Here, we use angle-resolved photoemission spectroscopy (ARPES) to study the recently reported quasi-freestanding bilayer graphene on a magnesium-terminated silicon carbide (SiC) substrate (Mg-QFSBLG) created by magnesium intercalation of epitaxial monolayer graphene on 6H-SiC [65]. Analysis of the electronic spectrum using a simple tight binding model indicates high n-doping ($>2 \times 10^{14}$ cm^{-2}). The exceptionally high displacement field produced by the charge transfer from the intercalated magnesium to graphene opens a large (0.36 eV) bandgap at the Dirac point. Moreover, the high level of n-doping is stable after heating to 350 °C, as well as 30 min of exposure to air. The electronic spectrum of the highly n-doped bilayer graphene is well described by a simple tight-binding model for bilayer graphene with displacement field. First-principles density-functional theory (DFT) calculations corroborate the finding that magnesium intercalation produces quasi-freestanding bilayer graphene with good agreement in doping level, Fermi energy, and bandgap to our experimental values.

2. Methods

Epitaxial monolayer graphene samples of nominally sub-monolayer coverage were grown on a silicon face of a semi-insulating 6H-SiC substrate by silicon sublimation from the SiC, as described in Ref. [66]. Sample preparation, ARPES, and low-energy electron diffraction (LEED) measurements were carried out at the Toroidal Analyzer endstation at the Soft X-ray Beamline of the Australian Synchrotron. Samples were introduced to ultra-high vacuum (UHV, base pressure of 1×10^{-10} mbar), and annealed over night at 500 °C. Sample cleanliness was confirmed by LEED and ARPES. A magnesium effusion cell was baked at 150 °C overnight and outgassed at 415 °C. Once the pressure reached 1×10^{-7} mbar, the effusion cell was inserted into the UHV preparation chamber. Magnesium (1/8 in. turnings, 99.95%, Sigma Aldrich) was intercalated following the recipe from Ref. [65]: Magnesium was evaporated for 25 min, with the magnesium cell held at 400 °C, and deposited on the graphene/SiC substrate held at room temperature in a thickness of 188 Å, as determined by quartz crystal microbalance. Following the deposition, the graphene/SiC substrate was annealed at 350 °C for 30 min to facilitate magnesium intercalation under the graphene buffer layer. For the air exposure experiment, the sample was reintroduced to UHV after 30 min of air exposure and annealed at 350 °C for several hours prior to measurements.

Structural characterisation of the samples was undertaken using LEED (OCI^{TM} 3 grid reverse view optics, 200 μm spot size) at room temperature, at energies between 56 eV and 200 eV, *in-situ* in the endstation used for ARPES. The ARPES measurements used a toroidal-type angle-resolving endstation [67] at the Soft X-Ray Beamline of the Australian Synchrotron. All ARPES data were taken at room temperature and with a photon energy ($h\upsilon$) of 100 eV using linearly polarised light at normal incidence to the sample, with a beam spot size of 100 μm × 60 μm. The binding energy (E_{Bin}) scales for all spectra are referenced to the Fermi energy (E_F), determined using the Fermi edge of an Au foil reference sample in electrical contact with the sample. The toroidal analyser permits all polar (θ) emission angles (−90° to +90°) to be measured along a high-symmetry azimuthal angle (φ) of the surface containing the $\overline{\Gamma}$ point. The unique geometry therefore allows for measurements of the Dirac cone along the $\overline{K}-\overline{\Gamma}-\overline{K}$ direction without the need for complex alignment of the spectrometer. A simple rotation of the sample in the azimuthal angle was then used to measure the Dirac point along the direction perpendicular to the $\overline{K}-\overline{\Gamma}-\overline{K}$ direction. Using this latter method avoids the well-known intensity suppression of half of the Dirac cone seen when measuring along the $\overline{K}-\overline{\Gamma}-\overline{K}$ direction using this polarization geometry [68] and provides a more robust means of determining the Dirac point and carrier velocities. The measurement direction perpendicular to the $\overline{K}-\overline{\Gamma}-\overline{K}$ direction; however, exhibits a lower $k_{||}$ instrumental resolution than in the $\overline{K}-\overline{\Gamma}-\overline{K}$ direction, resulting in higher-than-normal momentum broadening in the data. This effect is due to the finite-size analyser slit that is used when measuring the band structure along the azimuthal direction. The result is approximately an order of magnitude decrease in the instrumental angular resolution compared to scanning $k_{||}$ using the polar emission angle [67]. The contribution to the momentum uncertainty due to the angular resolution along φ is estimated to be ~0.1 Å^{-1}, compared with ~0.01 Å^{-1} for measurements taken along θ. In both measurement directions, however, the energy resolution is ~100 meV. Data taken along the $\overline{K}-\overline{\Gamma}-\overline{K}$ direction can be found in the Supplementary Material, section 2.

First-principles density-functional theory calculations were implemented using the Vienna ab initio Simulation Package (VASP) to calculate the electronic structure of Mg-QFSBLG [69]. The Perdew-Burke-Ernzehof (PBE) form of the generalized gradient approximation (GGA) was used to describe electron exchange and correlation [70]. A semi-empirical functional (DFT-D2) was employed to describe van der Waals interactions in the system [71]. The kinetic energy cut-off for the plane-wave basis set was set to 500 eV. We used a 9 × 9 × 1 Γ-centered k-point mesh for sampling the Brillouin zone. The unfolded band structure and Fermi surface were obtained using the KPROJ program based on the k-projection method [72,73].

3. Results and discussion

Intercalation is a method commonly used to tailor the properties of graphene [42–45,49–53,72–78]. The advent of epitaxial graphene on SiC has offered new opportunities for intercalation, as many species which will not intercalate graphite [79,80] will in fact intercalate the graphene-SiC interface [45,46,53,81,82] and alter the properties of the graphene overlayer(s). Magnesium is one such species which does not intercalate graphite [83], and therefore is not expected to intercalate in the galleries between graphene layers, but was recently observed to intercalate EMLG on SiC [65]. In this case, intercalation is possible due to the different chemical nature of the silicon-graphene interface, where

the silicon is bonded to the first carbon layer, known as the buffer layer (Fig. 1a). During the intercalation process, magnesium, rather than intercalating the graphene layer, goes under the buffer layer and sits on top of SiC, forming an Mg-silicide, as shown in Fig. 1b and demonstrated in Ref. [65]. Once magnesium is intercalated under the buffer layer, it effectively cuts the bonds between the carbon atoms in the buffer layer and silicon bonds, thus turning the buffer layer into a free graphene layer, and by extension transforming EMLG into Mg-QFSBLG.

LEED is used to confirm that EMLG is converted structurally to Mg-QFSBLG. Fig. 1c and 1d show LEED images before and after magnesium intercalation, respectively. Before intercalation, we observe the characteristic LEED pattern of EMLG, with the $(6\sqrt{3} \times 6\sqrt{3})R30^\circ$ reconstruction relative to the SiC lattice characteristic of the buffer layer (orange circles, Fig. 1c) in addition to the (1×1) graphene and (1×1) SiC spots (green and gray circles, respectively, Fig. 1c). After intercalation, the $(6\sqrt{3} \times 6\sqrt{3})R30^\circ$ spots are greatly reduced in intensity, and the graphene (1×1) spots are significantly more pronounced than the (1×1) SiC spots, indicating a reduced interaction with the substrate [64]. Additional $(\sqrt{3} \times \sqrt{3})R30^\circ$ spots with respect to the (1×1) SiC spots are visible (yellow circle, Fig. 1d) after intercalation and are attributed to the formation of the magnesium silicide-like surface reconstruction under the graphene [65]. The first-principles calculations support the interpretation that EMLG is converted to the Mg-QFSBLG heterostructure, shown in Fig. 1b, with the energy of the Mg-intercalated structure being lower than the energy of crystalline Mg on epitaxial monolayer graphene by 1.18 eV. Additional LEED data and more details on the calculation of the relative energies can be found in the Supplementary Material, section 1 and 5, respectively.

LEED itself, being a structural technique, cannot provide insight into the effect of magnesium intercalation on the electronic structure of graphene. To assess the electronic structure changes, a more direct probe of the electronic structure is needed. One such probe is the ARPES technique, which can directly visualise the electronic structure of materials and give information about doping, bandgap, number of layers, and many-body interactions [84,85].

Fig. 2 shows ARPES measurements, before and after magnesium intercalation. Fig. 2a and 2b show the Fermi surface (spectral weight as a function of in-plane momentum at constant energy at the Fermi level) of clean (non-intercalated) EMLG and Mg-QFSBLG, respectively. Here, the unique toroidal analyser geometry [67] enables the detection of a full hemisphere (i.e. a 180° photoelectron emission window), which samples a wide k-space. The differences in the Fermi surfaces are easily seen: Prior to the intercalation (Fig. 2a) the Fermi surface consists of an individual circular feature characteristic of the single Dirac cone of EMLG [86]. Following magnesium intercalation (Fig. 2b), an additional feature develops and two well-separated Fermi surfaces are clearly visible as a smaller circular feature enveloped by a larger triangular one. This is consistent with the bilayer graphene structure [13]. Note that the absence of the intensity on one side of the Fermi surface contour in the bilayer (and monolayer) graphene case is due to the interference effect from the two atoms in a graphene unit cell [68,86,87].

Fig. 2c and 2d show the band dispersion measured perpendicular to the $\overline{K} - \overline{\Gamma} - \overline{K}$ high-symmetry direction, as indicated schematically in the inset of Fig. 2c. This direction is chosen because there are no matrix-element effect-induced changes in the graphene band intensity along this vector. Before intercalation, Fig. 2c, a single set of linearly dispersing bands is visible, as expected for EMLG. The Dirac point position and Fermi velocity of $v_F = (1.17 \pm 0.02) \times 10^6$ m/s, a value similar to typically reported Fermi velocity for EMLG on SiC [88,89], were obtained from a linear fit (black line, Fig. 2c) to the band position values (blue markers) taken from the momentum distribution curves (MDCs). The Dirac point lies below the Fermi level, $E_F - E_D = 0.35 \pm$

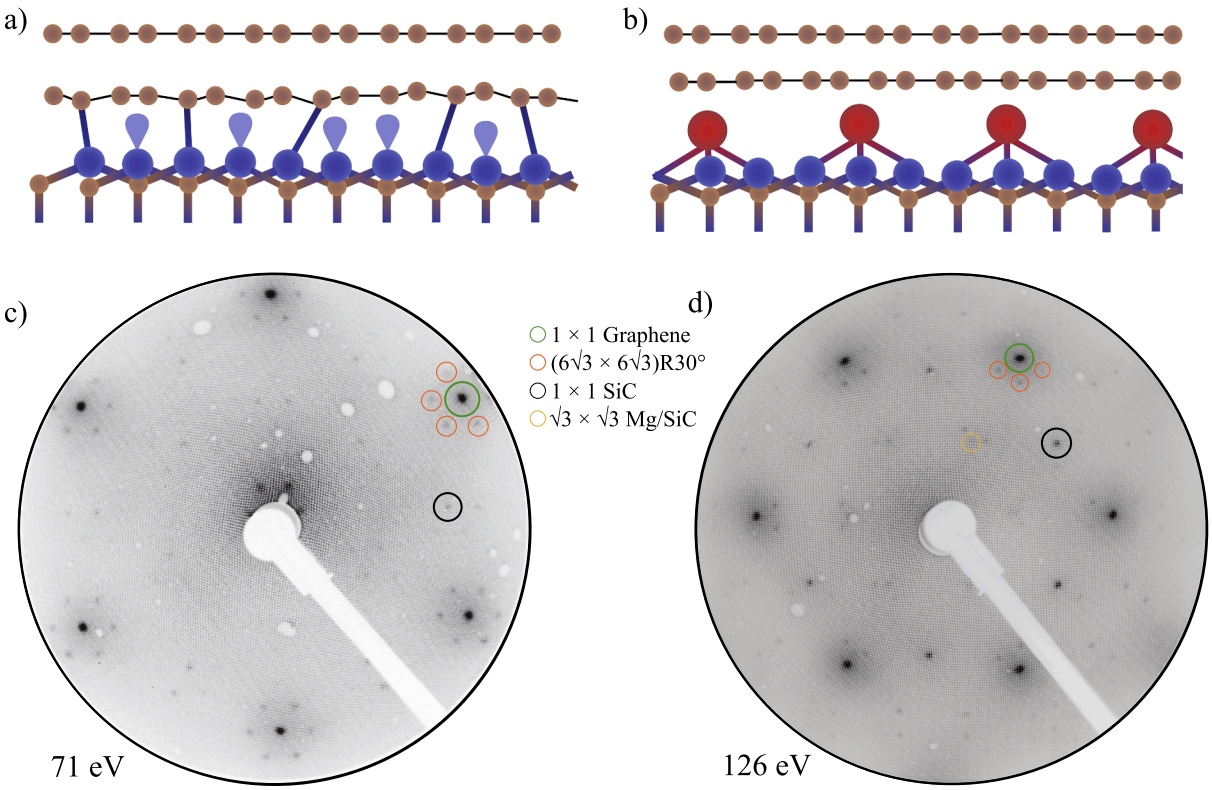

Fig. 1. Magnesium intercalated epitaxial monolayer graphene. Sketch of a) epitaxial monolayer graphene on SiC and b) magnesium-intercalated quasi-freestanding bilayer graphene on SiC. Brown spheres: carbon; blue spheres: silicon; blue lobes: silicon dangling bonds; red spheres: magnesium. LEED image of epitaxial monolayer c) before and d) after magnesium intercalation. LEED images taken at 71 eV and 126 eV, respectively, on the same sample. The sample was remounted between the LEED measurements. Green circle: (1×1) graphene lattice; gray circle: (1×1) SiC lattice; orange circles: $(6\sqrt{3} \times 6\sqrt{3})R30^\circ$ reconstruction relative to SiC arising from the buffer layer; yellow circle: $(\sqrt{3} \times \sqrt{3})$ R30° reconstruction of SiC surface by magnesium.

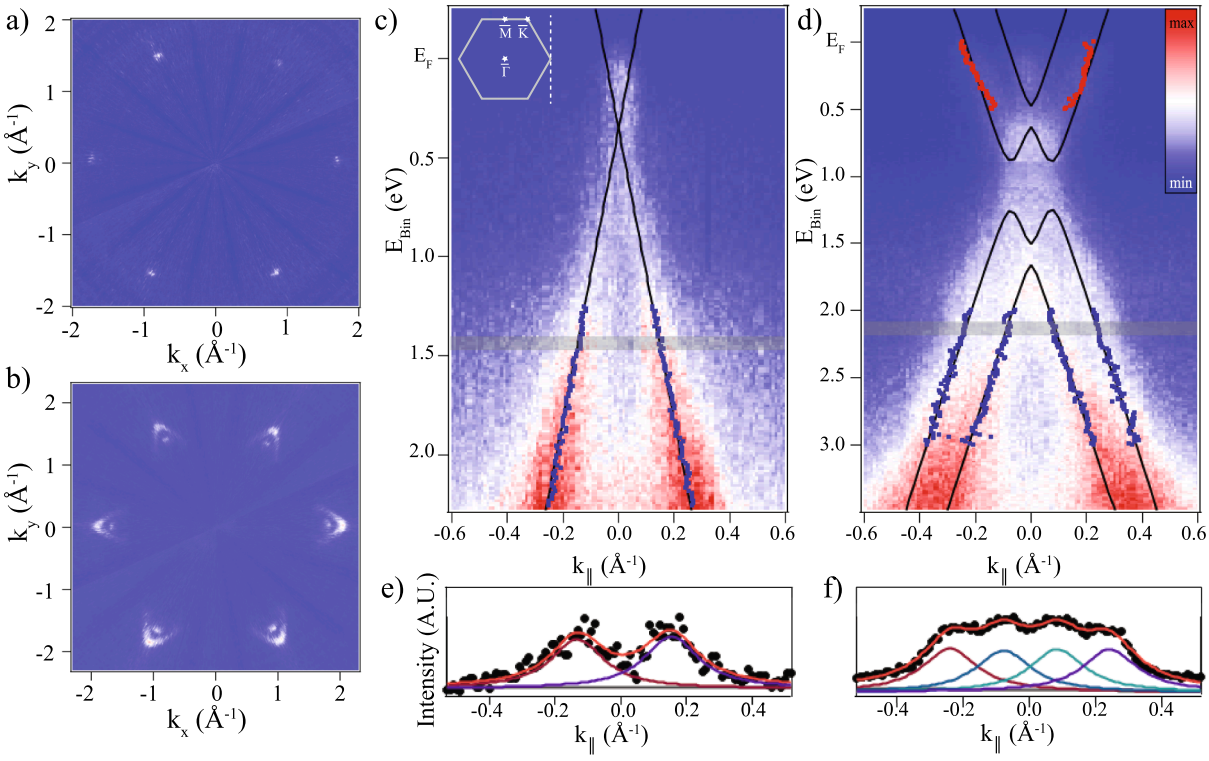

Fig. 2. Electronic structure of graphene on SiC before and after magnesium intercalation. Constant energy surfaces taken at the Fermi level showing a) monolayer graphene Fermi surface and b) bilayer graphene Fermi surface following magnesium intercalation. Band dispersion of c) monolayer graphene before and d) bilayer graphene after magnesium intercalation. Blue and red markers are extracted band positions from momentum distribution curves (MDCs). Overlaid in black are c) linear fit and d) tight-binding model for $U = 0.87$ V, defined in Eq.1 of the main text. e) and f) are extracted MDCs from the grey shaded area in c) and d), respectively, showing two (four) bands as expected for monolayer (bilayer) graphene. Bands were averaged in a 50 meV window, taken 1.1 eV below extrapolated Dirac point. All data taken at $hw = 100$ eV and at room temperature.

0.04 eV, an amount comparable to typical reported values for EMLG on SiC [37,64,75]. The Fermi wavevector, k_F, is determined to be 0.048 ± 0.004 Å^{-1}, corresponding to a carrier density of $n = (7.3 \pm 0.6) \times 10^{12}$ cm^{-2}.

After intercalation, Fig. 2d, two sets of bands are visible, as is expected for bilayer graphene. Red (blue) markers represent the conduction (valence) band position values obtained from the MDCs. These values were fitted to a tight-binding model, Eq. (1), overlaid in black, for bilayer graphene under a perpendicular displacement field, based on Refs. [13,14,90]:

$$\varepsilon_\alpha(k) = \pm\left[\frac{\gamma_1^2}{2} + \frac{U^2}{2} + \left(v^2 + \frac{v_3^2}{2}\right)k^2 + (-1)^\alpha\sqrt{\Psi}\right]^{1/2} \quad (1)$$

where α = 1,2 is the band index, and

$$\Psi = \frac{1}{4}(\gamma_1^2 - v_3^2k^2)^2 + v^2k^2\left(\gamma_1^2 + U^2 + v_3^2k^2\right) + 2\gamma_1 v_3 v^2 k^3 cos3\varphi$$

and $v_3 = \frac{\sqrt{3}a\gamma_3}{2\hbar}$.

Here, k is the wavevector, φ is the azimuthal angle, v is the band velocity, U is the difference in the onsite Coulomb potential of two graphene layers, $\gamma_1 = 0.4$ eV is the out-of-plane nearest-neighbour interaction parameter, $\gamma_3 = 0.12$ eV is the out-of-plane next-nearest-neighbour interaction parameter, $a = 1.42$ Å is the C-C distance in graphene, and ħ is reduced Planck's constant [13].

From the fit, we obtain a band gap value of $E_G = 0.36 \pm 0.04$ eV, which is in agreement with the theoretically predicted band gap for bilayer graphene under high displacement field [15], and $v = (0.97 \pm 0.04) \times 10^6$ m/s, which is of the same order of magnitude as in Ref. [13]. The tight-binding model includes an interlayer potential difference of 0.87 ± 0.06 V, yielding an extremely high displacement field of 2.6 ± 0.2 V/nm [91,92]. From the band parameters we obtain the Fermi wavevectors $k_{F,1} = 0.24 \pm 0.01$ Å^{-1} (outer band) and $k_{F,2} = 0.09 \pm 0.01$ Å^{-1} (inner band). We estimate the carrier densities as $n_i = 2k_{F,i}/\pi$ for i = 1,2. Note that the first-order correction to the Fermi wavevector due to trigonal warping is zero along the direction perpendicular to the $\overline{K} - \overline{\Gamma} - \overline{K}$ high-symmetry direction so this provides a good approximation even for the trigonally warped surface. We then find carrier densities $n_1 = (1.83 \pm 0.15) \times 10^{14}$ cm^{-2} (outer band) and $n_2 = (0.26 \pm 0.06) \times 10^{14}$ cm^{-2} (inner band), giving a total carrier density of $n = n_1 + n_2 = (2.1 \pm 0.2) \times 10^{14}$ cm^{-2}, and an interlayer difference in carrier density $n_1 - n_2 = (1.6 \pm 0.2) \times 10^{14}$ cm^{-2}.

It is expected that the interlayer potential difference responds linearly to the interlayer carrier density difference, i.e. $U = \alpha(n)(n_1 - n_2)$ where the linear response coefficient $\alpha(n)$ depends on the total carrier density n [93]. We observe $\alpha(n = (2.1 \pm 0.2) \times 10^{14}\,\text{cm}^{-2}) = (5.4 \pm 0.9) \times 10^{-12}$ meV cm^2. While $\alpha(n)$ has not to our knowledge been calculated from first-principles DFT at the very high carrier densities as in our experiment, Ref. [93] showed that calculation of $\alpha(n)$ using a GW approach gives excellent agreement with experiments at low n, and furthermore extrapolated their GW calculation analytically to high n. Using their extrapolation we find $\alpha(n = 2.1 \times 10^{14}\,\text{cm}^{-2}) = 5.9 \times 10^{-12}$ meV cm^2, in excellent agreement with our observation.

The extrapolated Dirac point position for the Mg-QFSBLG, $E_F - E_D$, is 1.07 ± 0.07 eV, corresponding to a Fermi level shift of 0.72 ± 0.08 eV with respect to the EMLG. Fig. 2e and 2f show MDCs obtained from the shaded areas (1.1 eV below the extrapolated Dirac point, bands averaged over a 50 meV binning window) in Fig. 2c and 2d, which clearly indicate the presence of two (four) bands, as expected for monolayer (bilayer) graphene. The total carrier density in our system is significantly higher (an order of magnitude) than in pristine bilayer graphene on SiC [94], and than in the previously reported air-stable n-doped

graphene systems [62,63], though higher densities have been achieved in vacuum for example by co-doping graphene by K and Ca [47], or by Cs [44] and Gd doping [45].

The electronic structure of the magnesium-intercalated sample obtained by ARPES measurements can be compared with the first-principles DFT calculations for a bilayer graphene system where magnesium atoms are sitting at the interface with the SiC substrate. The heterostructure is modelled using a ($\sqrt{3} \times \sqrt{3}$) SiC supercell and a (2×2) graphene supercell with one magnesium atom placed in between the two materials (Fig. 3a and 3b). The magnesium atom is located on the C-top location which is found to be stable and the most energetically favorable configuration (see Supplementary Material section 5 and Figure S9 for details). The lattice constant of SiC is unchanged while the graphene is stretched by 7.5%. We calculate the Fermi surface and electronic band structure of the system, Fig. 3c and 3d. The calculated Fermi surface (Fig. 3c) agrees well with our ARPES spectra, where two features are observed in the Fermi surface: A circular feature belonging to the top graphene layer conduction band (red contour lines), and a triangular one coming from the bottom layer conduction band (green contour lines). The DFT calculations also reproduce the experimental band dispersion as shown in Fig. 3d. The band gap is 0.35 eV, which is in excellent agreement with experimental observations. The doping level obtained from the calculations is 3.6×10^{14} cm^{-2}, somewhat larger than the experimental value of 2.1×10^{14} cm^{-2}, while the calculated Fermi energy relative to the Dirac point $E_F - E_D = 0.71$ eV is somewhat smaller than experimental value (1.07 eV). The differences are likely related to the artificial stretching of the graphene lattice by 7.5% which preserves the symmetry of the system but lowers the Fermi velocity by 10% relative to the true value [95].

Highly n-doped graphene/SiC has previously been achieved by depositing or intercalating alkali and alkali-earth metals on graphene [13,45–47,96], but the resulting systems are typically unstable when exposed to air. In our case, magnesium is buried between bilayer graphene and SiC, so it is conceivable that samples could survive air exposure. In order to test air stability, the magnesium-intercalated sample was taken out of UHV and exposed to air for 30 min.

Fig. 4a shows the Fermi surface measured by ARPES before and after 30 min air exposure. In both cases, the two clearly separated conduction bands of bilayer graphene are visible, with no significant change in the size of the Fermi surface (directly proportional to doping) after air exposure. Fig. 4b shows the electronic dispersion before and after 30 min air exposure. No significant changes are observed in the Fermi energy $E_F - E_D$, nor in the bandgap for our air exposed Mg-QFSBLG, within the experimental resolution. This degree of air stability is surprising for a surface layer and indicates that Mg-QFSBLG created by magnesium intercalation is relatively robust to ambient exposure, which is desirable for designing transparent conducting electrodes [5] with a low work function. Note that the sample used for the air exposure experiment was a different sample (EMLG with nominally 1 monolayer coverage) than the one for which data is shown in Fig. 1 and Fig. 2 due to the experimental time constraints. Full LEED and ARPES characterisation of this sample can be found in the Supplementary Material, section 3 and 4,

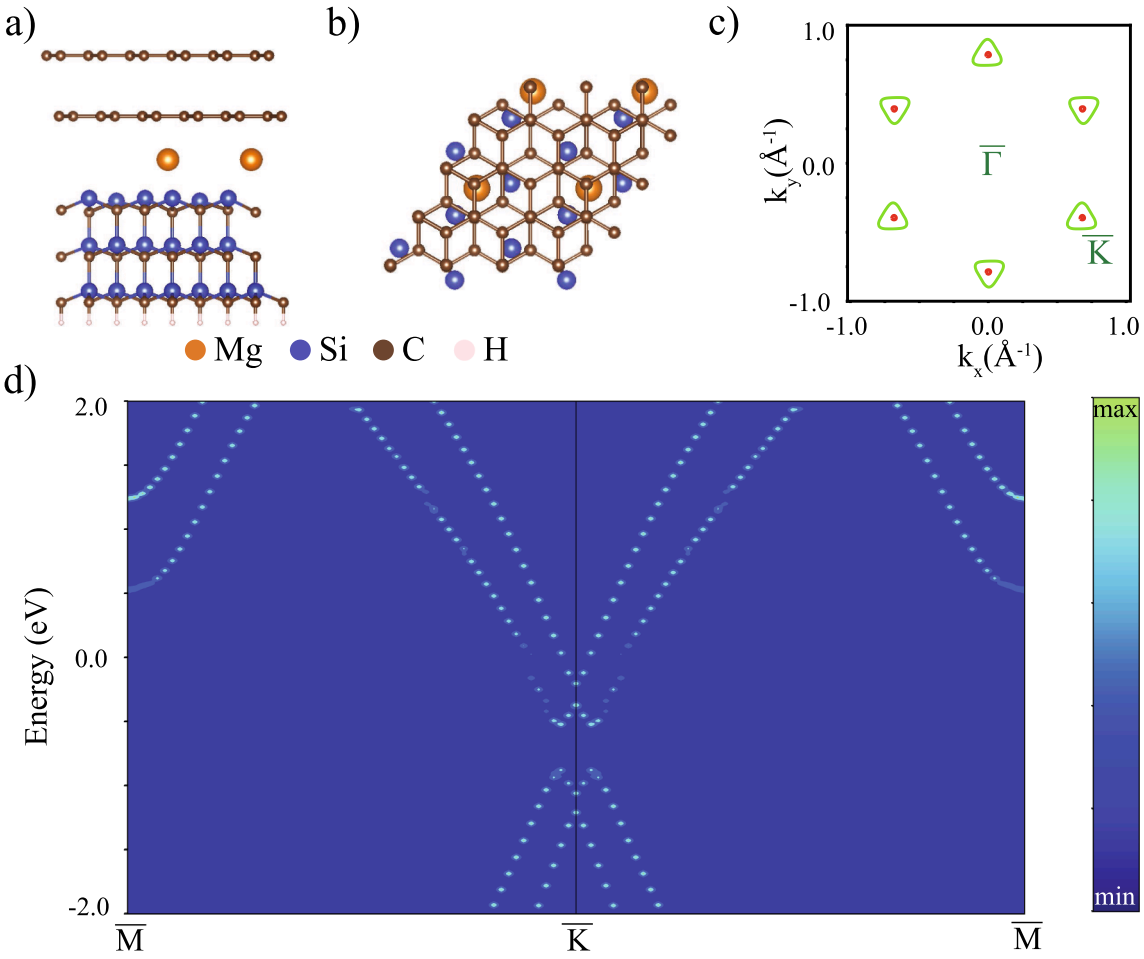

Fig. 3. First-principles DFT calculations of magnesium-intercalated bilayer graphene. Model used in DFT calculations: a) side view and b) top view of the graphene/magnesium/SiC interface. Brown, orange and blue spheres indicate the positions of carbon, magnesium and silicon atoms. Only the topmost silicon atoms of the SiC substrate are shown for clarity. c) Calculated unfolded constant energy slice at the Fermi level of magnesium-intercalated bilayer graphene. Red and green represent contributions from top and bottom graphene layer, respectively. d) Unfolded band dispersion of magnesium-intercalated bilayer graphene.

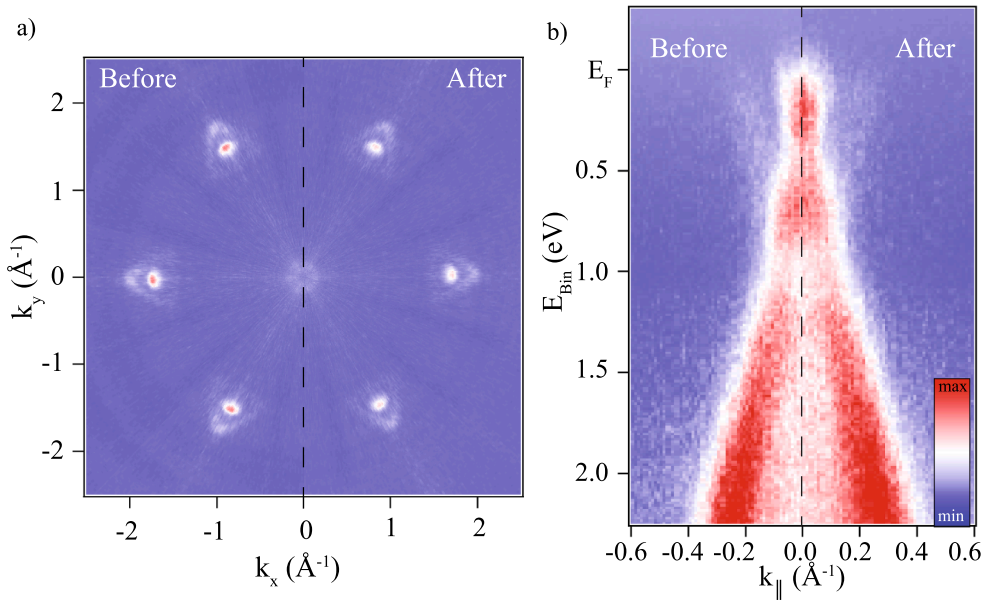

Fig. 4. Magnesium-intercalated epitaxial monolayer graphene before and after air exposure. Constant energy contours a) and background subtracted band dispersion b) of magnesium-intercalated sample before (left) and after (right) 30 min air exposure. Data taken at $h\nu = 100$ eV and at room temperature. Constant energy contour data was averaged around the $\overline{K}$ point to increase signal-to-noise ratio.

respectively.

4. Conclusions

We demonstrate that magnesium intercalation at the interface of SiC and the graphene buffer layer transforms epitaxial monolayer graphene into quasi-freestanding bilayer graphene, as observed by LEED and ARPES. Once at the interface, magnesium acts as an electron donor and dopes graphene, shifting the Fermi level by 0.72 eV and resulting in an electron carrier density of $n = 2.1 \times 10^{14}$ cm^{-2}, proportionate to the highest densities achievable with electrolytic gating (4×10^{14} cm^{-2}). Magnesium intercalation also creates an extremely high displacement field of 2.6 V/nm, comparable to the largest displacement fields (2.5–3.1 V/nm) obtained in dual gated bilayer graphene field-effect transistors. The field of 2.6 V/nm opens a bandgap of 0.36 eV, a value very close to γ_1 (out-of-plane nearest-neighbour interaction parameter) where the field-induced bandgap is expected to saturate, and increases the splitting between the valence (conduction) bands of bilayer graphene. Despite this extremely high displacement field, the electronic structure of the Mg-QFSBLG can still be described with a simple tight-binding model that well reproduces both the bandgap opening and the increase in the splitting between bands. First-principles DFT calculations are in good agreement and reproduce the experimental band structure well, including the bandgap opening and the increase in the band splitting. An air exposure test shows that the Mg-QFSBLG samples are stable in air for up to 30 min, and are thermodynamically stable up to at least 350 °C, suggesting that magnesium-intercalated graphene could be a suitable candidate for application in transparent electrodes and organic opto-electronics.

Author contributions

The manuscript was written through contributions of all authors. All authors have given approval to the final version of the manuscript.

CRediT authorship contribution statement

Antonija Grubišić-Čabo: Methodology, Software, Formal analysis, Investigation, Writing - original draft, Writing - review & editing, Visualization, Funding acquisition. **Jimmy C. Kotsakidis:** Conceptualization, Methodology, Investigation, Writing - review & editing, Funding acquisition. **Yuefeng Yin:** Methodology, Software, Formal analysis, Investigation, Visualization, Writing - review & editing. **Anton Tadich:** Methodology, Software, Formal analysis, Investigation, Writing - review & editing. **Matthew Haldon:** Investigation, Writing - review & editing. **Sean Solari:** Investigation, Writing - review & editing. **Iolanda Di Bernardo:** Investigation, Writing - review & editing. **Kevin M. Daniels:** Resources, Writing - review & editing. **John Riley:** Resources, Writing - review & editing. **Eric Huwald:** Resources, Writing - review & editing. **Mark T. Edmonds:** Investigation, Writing - review & editing, Funding acquisition. **Rachael Myers-Ward:** Resources, Writing - review & editing. **Nikhil V. Medhekar:** Methodology, Software, Supervision, Writing - review & editing, Funding acquisition. **D. Kurt Gaskill:** Resources, Supervision, Writing - review & editing, Funding acquisition. **Michael S. Fuhrer:** Methodology, Conceptualization, Formal analysis, Project administration, Supervision, Writing - review & editing, Funding acquisition.

Declaration of Competing Interest

The authors declare that they have no known competing financial interests or personal relationships that could have appeared to influence the work reported in this paper.

Acknowledgment

This work was supported by the Australian Research Council under awards DP150103837, DP200101345 and FL120100038. This research was undertaken on the Soft X-ray spectroscopy beamline at the Australian Synchrotron, part of ANSTO. JCK gratefully acknowledges support from the Australian Government Research Training Program, and the Monash Centre for Atomically Thin Materials. MH gratefully acknowledges support from the Monash University Summer Vacation Research Scholarship Program. SS gratefully acknowledges support from the Monash University Summer ResearchFirst Scholarships Program. YY and NM gratefully acknowledge the support from the Australian Research Council (CE17010039) and the computational support from the National Computing Infrastructure and Pawsey

Supercomputing Facilities. DKG, RMW, and KMD acknowledge support by core programs at the U.S. Naval Research Laboratory funded by the Office of Naval Research.

Appendix A. Supplementary material

Supplementary data to this article can be found online at https://doi.org/10.1016/j.apsusc.2020.148612.

References

[1] K.S. Novoselov, A.K. Geim, S.V. Morozov, D. Jiang, Y. Zhang, S.V. Dubonos, I. V. Grigorieva, A.A. Firsov, Electric field effect in atomically thin carbon films, Science 80 (2004) 306666–306669, https://doi.org/10.1126/science.1102896.

[2] J.-H. Chen, C. Jang, S. Xiao, M. Ishigami, M.S. Fuhrer, Intrinsic and extrinsic performance limits of graphene devices on SiO_2, Nat. Nanotechnol. 3 (2008) 206–209, https://doi.org/10.1038/nnano.2008.58.

[3] R.R. Nair, P. Blake, A.N. Grigorenko, K.S. Novoselov, T.J. Booth, T. Stauber, N.M. R. Peres, A.K. Geim, Fine structure constant defines visual transparency of graphene, Science 80 (2008) 3201308, https://doi.org/10.1126/science.1156965.

[4] I. Khrapach, F. Withers, T.H. Bointon, D.K. Polyushkin, W.L. Barnes, S. Russo, M. F. Craciun, Novel highly conductive and transparent graphene-based conductors, Adv. Mater. 24 (2012) 2844–2849, https://doi.org/10.1002/adma.201200489.

[5] W. Bao, J. Wan, X. Han, X. Cai, H. Zhu, D. Kim, D. Ma, Y. Xu, J.N. Munday, H. D. Drew, M.S. Fuhrer, L. Hu, Approaching the limits of transparency and conductivity in graphitic materials through lithium intercalation, Nat. Commun. 5 (2014) 4224, https://doi.org/10.1038/ncomms5224.

[6] Y.-J. Yu, Y. Zhao, S. Ryu, L.E. Brus, K.S. Kim, P. Kim, Tuning the graphene work function by electric field effect, Nano Lett. 9 (2009) 3430–3434, https://doi.org/10.1021/nl901572a.

[7] H. Yang, J. Heo, S. Park, H.J. Song, D.H. Seo, K.-E. Byun, P. Kim, I. Yoo, H.-J. Chung, K. Kim, Graphene barristor, a triode device with a gate-controlled Schottky barrier, Science 80 (2012) 3361140–3361143, https://doi.org/10.1126/science.1220527.

[8] X. Cui, G.-H. Lee, Y.D. Kim, G. Arefe, P.Y. Huang, C.-H. Lee, D.A. Chenet, X. Zhang, L. Wang, F. Ye, F. Pizzocchero, B.S. Jessen, K. Watanabe, T. Taniguchi, D.A. Muller, T. Low, P. Kim, J. Hone, Multi-terminal transport measurements of MoS2 using a van der Waals heterostructure device platform, Nat. Nanotechnol. 10 (2015) 534–540, https://doi.org/10.1038/nnano.2015.70.

[9] F. Wang, Y. Zhang, C. Tian, C. Girit, A. Zettl, M. Crommie, Y.R. Shen, Gate-variable optical transitions in graphene, Science 80 (2008) 320206–320209, https://doi.org/10.1126/science.1152793.

[10] Y. Chen, Y.-Y. Yue, S.-R. Wang, N. Zhang, J. Feng, H.-B. Sun, Graphene as a transparent and conductive electrode for organic optoelectronic devices, Adv. Electron. Mater. 5 (2019) 1900247, https://doi.org/10.1002/aelm.201900247.

[11] E. McCann, V.I. Fal'ko, Landau-level degeneracy and quantum hall effect in a graphite bilayer, Phys. Rev. Lett. 96 (2006) 1–4, https://doi.org/10.1103/PhysRevLett.96.086805.

[12] K.S. Novoselov, E. McCann, S.V. Morozov, V.I. Fal'ko, M.I. Katsnelson, U. Zeitler, D. Jiang, F. Schedin, A.K. Geim, Unconventional quantum Hall effect and Berry's phase of 2π in bilayer graphene, Nat. Phys. 2 (2006) 177–180, https://doi.org/10.1038/nphys245.

[13] T. Ohta, A. Bostwick, T. Seyller, K. Horn, E. Rotenberg, Controlling the electronic structure of bilayer graphene, Science 80 (2006) 313951–313954, https://doi.org/10.1126/science.1130681.

[14] E. McCann, Asymmetry gap in the electronic band structure of bilayer graphene, Phys. Rev. B. 74 (2006), 161403, https://doi.org/10.1103/PhysRevB.74.161403.

[15] H. Min, B. Sahu, S.K. Banerjee, A.H. MacDonald, Ab initio theory of gate induced gaps in graphene bilayers, Phys. Rev. B. 75 (2007), 155115, https://doi.org/10.1103/PhysRevB.75.155115.

[16] E.V. Castro, K.S. Novoselov, S.V. Morozov, N.M.R. Peres, J.M.B.L. dos Santos, J. Nilsson, F. Guinea, A.K. Geim, A.H.C. Neto, Biased bilayer graphene: semiconductor with a gap tunable by the electric field effect, Phys. Rev. Lett. 99 (2007), 216802, https://doi.org/10.1103/PhysRevLett.99.216802.

[17] J.B. Oostinga, H.B. Heersche, X. Liu, A.F. Morpurgo, L.M.K. Vandersypen, Gate-induced insulating state in bilayer graphene devices, Nat. Mater. 7 (2008) 151–157, https://doi.org/10.1038/nmat2082.

[18] Y. Zhang, T.-T. Tang, C. Girit, Z. Hao, M.C. Martin, A. Zettl, M.F. Crommie, Y. R. Shen, F. Wang, Direct observation of a widely tunable bandgap in bilayer graphene, Nature 459 (2009) 820–823, https://doi.org/10.1038/nature08105.

[19] K.F. Mak, C.H. Lui, J. Shan, T.F. Heinz, Observation of an electric-field-induced band gap in bilayer graphene by infrared spectroscopy, Phys. Rev. Lett. 102 (2009), 256405, https://doi.org/10.1103/PhysRevLett.102.256405.

[20] J.G. Oh, K. Pak, C.S. Kim, J.H. Bong, W.S. Hwang, S.G. Im, B.J. Cho, A high-performance top-gated graphene field-effect transistor with excellent flexibility enabled by an iCVD copolymer gate dielectric, Small 14 (2018) 1–8, https://doi.org/10.1002/smll.201703035.

[21] M.C. Lemme, S. Member, T.J. Echtermeyer, M. Baus, H. Kurz, A graphene field-effect device, IEEE Electron Device Lett. 28 (2007) 282–284, https://doi.org/10.1109/LED.2007.891668.

[22] X. Xu, C. Wang, Y. Liu, X. Wang, N. Gong, Z. Zhu, B. Shi, M. Ren, W. Cai, R.A. Rupp, X. Zhang, J. Xu, A graphene P-N junction induced by single-gate control of dielectric structures, J. Mater. Chem. C. 7 (2019) 8796–8802, https://doi.org/10.1039/c9tc02474c.

[23] F.W. Chen, H. Ilatikhameneh, G. Klimeck, Z. Chen, R. Rahman, Configurable electrostatically doped high performance bilayer graphene tunnel FET, IEEE J. Electron Devices Soc. 4 (2016) 124–128, https://doi.org/10.1109/JEDS.2016.2539919.

[24] B.N. Szafranek, G. Fiori, D. Schall, D. Neumaier, H. Kurz, Current saturation and voltage gain in bilayer graphene field effect transistors, Nano Lett. 12 (2012) 1324–1328, https://doi.org/10.1021/nl2038634.

[25] K. Xu, H. Lu, E.W. Kinder, A. Seabaugh, S.K. Fullerton-Shirey, Monolayer solid-state electrolyte for electric double layer gating of graphene field-effect transistors, ACS Nano 11 (2017) 5453–5464, https://doi.org/10.1021/acsnano.6b08505.

[26] K. Xu, J. Liang, A. Woeppel, M.E. Bostian, H. Ding, Z. Chao, J.R. McKone, E. J. Beckman, S.K. Fullerton-Shirey, Electric double-layer gating of two-dimensional field-effect transistors using a single-ion conductor, ACS Appl. Mater. Interfaces. 11 (2019) 35879–35887, https://doi.org/10.1021/acsami.9b11526.

[27] C.K. Hayashi, D.G. Garmire, T.J. Yamauchi, C.M. Torres, R.C. Ordonez, High on-off ratio graphene switch via electrical double layer gating, IEEE Access 8 (2020) 92314–92321, https://doi.org/10.1109/ACCESS.2020.2994611.

[28] D.K. Efetov, P. Kim, Controlling electron-phonon interactions in graphene at ultrahigh carrier densities, Phys. Rev. Lett. 105 (2010), 256805, https://doi.org/10.1103/PhysRevLett.105.256805.

[29] R. Campos, J. Borme, J.R. Guerreiro, G. Machado, M.F. Cerqueira, D.Y. Petrovykh, P. Alpuim, Attomolar label-free detection of dna hybridization with electrolyte-gated graphene field-effect transistors, ACS Sensors 4 (2019) 286–293, https://doi.org/10.1021/acssensors.8b00344.

[30] M. Son, H. Kim, J. Jang, S.Y. Kim, H.C. Ki, B.H. Lee, I.S. Kim, M.H. Ham, Low-power complementary logic circuit using polymer-electrolyte-gated graphene switching devices, ACS Appl. Mater. Interfaces. 11 (2019) 47247–47252, https://doi.org/10.1021/acsami.9b16417.

[31] J. Xiao, H. Zhan, X. Wang, Z.Q. Xu, Z. Xiong, K. Zhang, G.P. Simon, J.Z. Liu, D. Li, Electrolyte gating in graphene-based supercapacitors and its use for probing nanoconfined charging dynamics, Nat. Nanotechnol. (2020), https://doi.org/10.1038/s41565-020-0704-7.

[32] R. Lv, Q. Li, A.R. Botello-Méndez, T. Hayashi, B. Wang, A. Berkdemir, Q. Hao, A. L. Eléas, R. Cruz-Silva, H.R. Gutiérrez, Y.A. Kim, H. Muramatsu, J. Zhu, M. Endo, H. Terrones, J.C. Charlier, M. Pan, M. Terrones, Nitrogen-doped graphene: Beyond single substitution and enhanced molecular sensing, Sci. Rep. 2 (2012) 1–8, https://doi.org/10.1038/srep00586.

[33] H. Wang, Q. Wang, Y. Cheng, K. Li, Y. Yao, Q. Zhang, C. Dong, P. Wang, U. Schwingenschlögl, W. Yang, X.X. Zhang, Doping monolayer graphene with single atom substitutions, Nano Lett. 12 (2012) 141–144, https://doi.org/10.1021/nl2031629.

[34] M. Rafique, Y. Shuai, I. Ahmed, R. Shaikh, M.A. Tunio, Tailoring electronic and optical parameters of bilayer graphene through boron and nitrogen atom co-substitution; an ab-initio study, Appl. Surf. Sci. 480 (2019) 463–471, https://doi.org/10.1016/j.apsusc.2019.02.240.

[35] H. Inani, K. Mustonen, A. Markevich, E.X. Ding, M. Tripathi, A. Hussain, C. Mangler, E.I. Kauppinen, T. Susi, J. Kotakoski, Silicon substitution in nanotubes and graphene via intermittent vacancies, J. Phys. Chem. C. 123 (2019) 13136–13140, https://doi.org/10.1021/acs.jpcc.9b01894.

[36] C.R.S.V. Boas, B. Focassio, E. Marinho, D.G. Larrude, M.C. Salvadori, C.R. Leão, D. J. dos Santos, Characterization of nitrogen doped graphene bilayers synthesized by fast, low temperature microwave plasma-enhanced chemical vapour deposition, Sci. Rep. 9 (2019) 1–12, https://doi.org/10.1038/s41598-019-49900-9.

[37] A. Tadich, M.T. Edmonds, L. Ley, F. Fromm, Y. Smets, Z. Mazej, J. Riley, C.I. Pakes, T. Seyller, M. Wanke, Tuning the charge carriers in epitaxial graphene on SiC (0001) from electron to hole via molecular doping with C60F48, Appl. Phys. Lett. 102 (2013), 241601, https://doi.org/10.1063/1.4811248.

[38] B.N. Szafranek, D. Schall, M. Otto, D. Neumaier, H. Kurz, High on/off ratios in bilayer graphene field effect transistors realized by surface dopants, Nano Lett. 11 (2011) 2640–2643, https://doi.org/10.1021/nl200631m.

[39] P. Solís-Fernández, S. Okada, T. Sato, M. Tsuji, H. Ago, Gate-tunable dirac point of molecular doped graphene, ACS Nano 10 (2016) 2930–2939, https://doi.org/10.1021/acsnano.6b00064.

[40] K. Iyakutti, E.M. Kumar, I. Lakshmi, R. Thapa, R. Rajeswarapalanichamy, V. J. Surya, Y. Kawazoe, Effect of surface doping on the band structure of graphene: a DFT study, J. Mater. Sci. Mater. Electron. 27 (2016) 2728–2740, https://doi.org/10.1007/s10854-015-4083-z.

[41] E. Zhou, J. Xi, Y. Liu, Z. Xu, Y. Guo, L. Peng, W. Gao, J. Ying, Z. Chen, C. Gao, Large-area potassium-doped highly conductive graphene films for electromagnetic interference shielding, Nanoscale 9 (2017) 18613–18618, https://doi.org/10.1039/c7nr07030f.

[42] T.-H. Han, S.-J. Kwon, N. Li, H.-K. Seo, W. Xu, K.S. Kim, T.-W. Lee, Versatile p-type chemical doping to achieve ideal flexible graphene electrodes, Angew. Chemie. 128 (2016) 6305–6309, https://doi.org/10.1002/ange.201600414.

[43] A.L. Jørgensen, D.A. Duncan, C.F.P. Kastorp, L. Kyhl, Z. Tang, A. Bruix, M. Andersen, B. Hammer, T.L. Lee, L. Hornekær, R. Balog, Chemically-resolved determination of hydrogenated graphene-substrate interaction, Phys. Chem. Chem. Phys. 21 (2019) 13462–13466, https://doi.org/10.1039/c9cp02059d.

[44] N. Ehlen, M. Hell, G. Marini, E.H. Hasdeo, R. Saito, Y. Falke, M.O. Goerbig, G. Di Santo, L. Petaccia, G. Profeta, A. Grüneis, Origin of the flat band in heavily Cs-doped graphene, ACS Nano 14 (2020) 1055–1069, https://doi.org/10.1021/acsnano.9b08622.

[45] S. Link, S. Forti, A. Stöhr, K. Küster, M. Rösner, D. Hirschmeier, C. Chen, J. Avila, M.C. Asensio, A.A. Zakharov, T.O. Wehling, A.I. Lichtenstein, M.I. Katsnelson,

U. Starke, Introducing strong correlation effects into graphene by gadolinium intercalation, Phys. Rev. B. 100 (2019), 121407, https://doi.org/10.1103/PhysRevB.100.121407.
[46] S. Watcharinyanon, L.I. Johansson, C. Xia, J. Ingo Flege, A. Meyer, J. Falta, C. Virojanadara, Ytterbium intercalation of epitaxial graphene grown on Si-face SiC, Graphene 2 (2013) 66–73, https://doi.org/10.4236/graphene.2013.22010.
[47] J.L. McChesney, A. Bostwick, T. Ohta, T. Seyller, K. Horn, J. González, E. Rotenberg, Extended van hove singularity and superconducting instability in doped graphene, Phys. Rev. Lett. 104 (2010), 136803, https://doi.org/10.1103/PhysRevLett.104.136803.
[48] S. Ichinokura, K. Sugawara, A. Takayama, T. Takahashi, S. Hasegawa, Superconducting calcium-intercalated bilayer graphene, ACS Nano 10 (2016) 2761–2765, https://doi.org/10.1021/acsnano.5b07848.
[49] S. Günther, T.O. Menteş, R. Reichelt, E. Miniussi, B. Santos, A. Baraldi, A. Locatelli, Au intercalation under epitaxial graphene on Ru(0001): the role of graphene edges, Carbon 162 (2020) 292–299, https://doi.org/10.1016/j.carbon.2020.02.025.
[50] Y. Dedkov, E. Voloshina, Spectroscopic and DFT studies of graphene intercalation systems on metals, J. Electron Spectros. Relat. Phenomena. 219 (2017) 77–85, https://doi.org/10.1016/j.elspec.2016.11.012.
[51] L. Daukiya, M.N. Nair, S. Hajjar-Garreau, F. Vonau, D. Aubel, J.L. Bubendorff, M. Cranney, E. Denys, A. Florentin, G. Reiter, L. Simon, Highly n -doped graphene generated through intercalated terbium atoms, Phys. Rev. B. 97 (2018) 2–7, https://doi.org/10.1103/PhysRevB.97.035309.
[52] J.P. Bonacum, A. O'Hara, D.L. Bao, O.S. Ovchinnikov, Y.F. Zhang, G. Gordeev, S. Arora, S. Reich, J.C. Idrobo, R.F. Haglund, S.T. Pantelides, K.I. Bolotin, Atomic-resolution visualization and doping effects of complex structures in intercalated bilayer graphene, Phys. Rev. Mater. 3 (2019) 1–10, https://doi.org/10.1103/PhysRevMaterials.3.064004.
[53] P. Rosenzweig, H. Karakachian, S. Link, K. Küster, U. Starke, Tuning the doping level of graphene in the vicinity of the Van Hove singularity via ytterbium intercalation, Phys. Rev. B. 100 (2019) 35445, https://doi.org/10.1103/PhysRevB.100.035445.
[54] P. Braeuninger-Weimer, O. Burton, R.S. Weatherup, R. Wang, P. Dudin, B. Brennan, A.J. Pollard, B.C. Bayer, V.P. Veigang-Radulescu, J.C. Meyer, B. J. Murdoch, P.J. Cumpson, S. Hofmann, Reactive intercalation and oxidation at the buried graphene-germanium interface, APL Mater. 7 (2019), https://doi.org/10.1063/1.5098351.
[55] H. Guo, R. Zhang, H. Li, X. Wang, H. Lu, K. Qian, G. Li, L. Huang, X. Lin, Y. Y. Zhang, H. Ding, S. Du, S.T. Pantelides, H.J. Gao, Sizable band gap in epitaxial bilayer graphene induced by silicene intercalation, Nano Lett. 20 (2020) 2674–2680, https://doi.org/10.1021/acs.nanolett.0c00306.
[56] I. Antoniazzi, T. Chagas, M.J.S. Matos, L.A.B. Marçal, E.A. Soares, M.S.C. Mazzoni, R.H. Miwa, J.M.J. Lopes, Â. Malachias, R. Magalhães-Paniago, M.H. Oliveira, Oxygen intercalated graphene on SiC(0001): multiphase SiOx layer formation and its influence on graphene electronic properties, Carbon 167 (2020) 746–759, https://doi.org/10.1016/j.carbon.2020.05.064.
[57] N. Briggs, B. Bersch, Y. Wang, J. Jiang, R.J. Koch, N. Nayir, K. Wang, M. Kolmer, W. Ko, A. De La Fuente Duran, S. Subramanian, C. Dong, J. Shallenberger, M. Fu, Q. Zou, Y.W. Chuang, Z. Gai, A.P. Li, A. Bostwick, C. Jozwiak, C.Z. Chang, E. Rotenberg, J. Zhu, A.C.T. van Duin, V. Crespi, J.A. Robinson, Atomically thin half-van der Waals metals enabled by confinement heteroepitaxy, Nat. Mater. 19 (2020) 637–643, https://doi.org/10.1038/s41563-020-0631-x.
[58] D.J. Wehenkel, T.H. Bointon, T. Booth, P. Bøggild, M.F. Craciun, S. Russo, Unforeseen high temperature and humidity stability of FeCl3 intercalated few layer graphene, Sci. Rep. 5 (2015) 1–5, https://doi.org/10.1038/srep07609.
[59] S.J. Kwon, T.H. Han, T.Y. Ko, N. Li, Y. Kim, D.J. Kim, S.H. Bae, Y. Yang, B.H. Hong, K.S. Kim, S. Ryu, T.W. Lee, Extremely stable graphene electrodes doped with macromolecular acid, Nat. Commun. 9 (2018) 1–9, https://doi.org/10.1038/s41467-018-04385-4.
[60] A. Piazza, F. Giannazzo, G. Buscarino, G. Fisichella, A. La Magna, F. Roccaforte, M. Cannas, F.M. Gelardi, S. Agnello, Graphene p-type doping and stability by thermal treatments in molecular oxygen controlled atmosphere, J. Phys. Chem. C. 119 (2015) 22718–22723, https://doi.org/10.1021/acs.jpcc.5b07301.
[61] K. Kanahashi, N. Tanaka, Y. Shoji, M. Maruyama, I. Jeon, K. Kawahara, M. Ishihara, M. Hasegawa, H. Ohta, H. Ago, Y. Matsuo, S. Okada, T. Fukushima, T. Takenobu, Formation of environmentally stable hole-doped graphene films with instantaneous and high-density carrier doping via a boron-based oxidant, Npj 2D Mater Appl. 3 (2019) 1–7, https://doi.org/10.1038/s41699-019-0090-x.
[62] S. Sanders, A. Cabrero-Vilatela, P.R. Kidambi, J.A. Alexander-Webber, C. Weijtens, P. Braeuninger-Weimer, A.I. Aria, M.M. Qasim, T.D. Wilkinson, J. Robertson, S. Hofmann, J. Meyer, Engineering high charge transfer n-doping of graphene electrodes and its application to organic electronics, Nanoscale 7 (2015) 13135–13142, https://doi.org/10.1039/C5NR03246F.
[63] K.S. Han, P.Y. Kalode, Y.-E. Koo Lee, H. Kim, L. Lee, M.M. Sung, A non-destructive n-doping method for graphene with precise control of electronic properties via atomic layer deposition, Nanoscale 8 (2016) 5000–5005, https://doi.org/10.1039/C5NR08016A.
[64] C. Riedl, C. Coletti, U. Starke, Structural and electronic properties of epitaxial graphene on SiC(0001): a review of growth, characterization, transfer doping and hydrogen intercalation, J. Phys. D. Appl. Phys. 43 (2010), 374009, https://doi.org/10.1088/0022-3727/43/37/374009.
[65] J.C. Kotsakidis, A. Grubišić-Čabo, Y. Yin, A. Tadich, R. Myers-Ward, M.T. DeJarld, S.P. Pavunny, M. Currie, K. Daniels, C. Liu, M.T. Edmonds, N.V. Medhekar, D. K. Gaskill, A.L. de Parga, M.S. Fuhrer, Freestanding n-doped graphene via intercalation of calcium and magnesium into the buffer layer - SiC(0001) interface, Chem. Mater. 32 (2020) 64646482, https://doi.org/10.1021/acs.chemmater.0c01729.
[66] L.O. Nyakiti, V.D. Wheeler, N.Y. Garces, R.L. Myers-Ward, C.R. Eddy Jr., D. K. Gaskill, Enabling graphene-based technologies: toward wafer-scale production of epitaxial graphene, MRS Bull. 37 (2012) 1149–1157, https://doi.org/10.1557/mrs.2012.180.
[67] L. Broekman, A. Tadich, E. Huwald, J. Riley, R. Leckey, T. Seyller, K. Emtsev, L. Ley, First results from a second generation toroidal electron spectrometer, J. Electron Spectros. Relat. Phenomena. 144–147 (2005) 1001–1004, https://doi.org/10.1016/j.elspec.2005.01.022.
[68] M. Mucha-Kruczyński, O. Tsyplyatyev, A. Grishin, E. McCann, V.I. Fal'ko, A. Bostwick, E. Rotenberg, Characterization of graphene through anisotropy of constant-energy maps in angle-resolved photoemission, Phys. Rev. B 77 (2008) 195403, https://doi.org/10.1103/PhysRevB.77.195403.
[69] G. Kresse, J. Furthmüller, Efficiency of ab-initio total energy calculations for metals and semiconductors using a plane-wave basis set, Comput. Mater. Sci. 6 (1996) 15–50, https://doi.org/10.1016/0927-0256(96)00008-0.
[70] J.P. Perdew, K. Burke, M. Ernzerhof, Generalized gradient approximation made simple, Phys. Rev. Lett. 77 (1996) 3865–3868, https://doi.org/10.1103/PhysRevLett.77.3865.
[71] S. Grimme, S. Ehrlich, L. Goerigk, Effect of the damping function in dispersion corrected density functional theory, J. Comput. Chem. 32 (2011) 1456–1465, https://doi.org/10.1002/jcc.21759.
[72] M. Chen, M. Weinert, Layer k-projection and unfolding electronic bands at interfaces, Phys. Rev. B. 98 (2018), 245421, https://doi.org/10.1103/PhysRevB.98.245421.
[73] M.X. Chen, W. Chen, Z. Zhang, M. Weinert, Effects of magnetic dopants in (Li0.8M0.2OH) FeSe (M=Fe, Mn, Co): Density functional theory study using a band unfolding technique, Phys. Rev. B. 96 (2017), 245111, https://doi.org/10.1103/PhysRevB.96.245111.
[74] C. Riedl, C. Coletti, T. Iwasaki, A.A. Zakharov, U. Starke, Quasi-free-standing epitaxial graphene on SiC obtained by hydrogen intercalation, Phys. Rev. Lett. 103 (2009) 1–4, https://doi.org/10.1103/PhysRevLett.103.246804.
[75] N. Briggs, Z.M. Gebeyehu, A. Vera, T. Zhao, K. Wang, A. De La Fuente Duran, B. Bersch, T. Bowen, K.L. Knappenberger, J.A. Robinson, Epitaxial graphene/silicon carbide intercalation: a minireview on graphene modulation and unique 2D materials, Nanoscale 11 (2019) 15440–15447, https://doi.org/10.1039/c9nr03721g.
[76] R. Balog, A. Cassidy, J. Jørgensen, L. Kyhl, M. Andersen, A.G. Čabo, F. Ravani, L. Bignardi, P. Lacovig, S. Lizzit, L. Hornekær, Hydrogen interaction with graphene on Ir(1 1 1): a combined intercalation and functionalization study, J. Phys. Condens. Matter. 31 (2019), https://doi.org/10.1088/1361-648X/aaf76b.
[77] A. Yurtsever, J. Onoda, T. Iimori, K. Niki, T. Miyamachi, M. Abe, S. Mizuno, S. Tanaka, F. Komori, Y. Sugimoto, Effects of Pb intercalation on the structural and electronic properties of epitaxial graphene on SiC, Small (2016) 3956–3966, https://doi.org/10.1002/smll.201600666.
[78] A.E. Mansour, A.R. Kirmani, S. Barlow, S.R. Marder, A. Amassian, Hybrid doping of few-layer graphene via a combination of intercalation and surface doping, ACS Appl. Mater. Interfaces. 9 (2017) 20020–20028, https://doi.org/10.1021/acsami.7b02886.
[79] J. Xu, Y. Dou, Z. Wei, J. Ma, Y. Deng, Y. Li, H. Liu, S. Dou, Recent progress in graphite intercalation compounds for rechargeable metal (Li, Na, K, Al)-ion batteries, Adv. Sci. 4 (2017) 1700146, https://doi.org/10.1002/advs.201700146.
[80] M.S. Dresselhaus, G. Dresselhaus, Intercalation compounds of graphite, Adv. Phys. 51 (2002) 1–186, https://doi.org/10.1080/00018730110113644.
[81] K.V. Emtsev, A.A. Zakharov, C. Coletti, S. Forti, U. Starke, Ambipolar doping in quasifree epitaxial graphene on SiC(0001) controlled by Ge intercalation, Phys. Rev. B. 84 (2011) 1–6, https://doi.org/10.1103/PhysRevB.84.125423.
[82] H. Kim, O. Dugerjav, A. Lkhagvasuren, J.M. Seo, Origin of ambipolar graphene doping induced by the ordered Ge film intercalated on SiC(0001), Carbon 108 (2016) 154–164, https://doi.org/10.1016/j.carbon.2016.07.010.
[83] Y. Liu, B.V. Merinov, W.A. Goddard, Origin of low sodium capacity in graphite and generally weak substrate binding of Na and Mg among alkali and alkaline earth metals, Proc. Natl. Acad. Sci. U.S.A. 113 (2016) 3735–3739, https://doi.org/10.1073/pnas.1602473113.
[84] S. Hüffner, Photoelectron Spectroscopy, Springer 3rd ed., ISBN 978-3-662-09280-4.
[85] A. Damascelli, Z. Hussain, Z.-X. Shen, Angle-resolved photoemission studies of the cuprate superconductors, Rev. Mod. Phys. 75 (2003) 473–541, https://doi.org/10.1103/RevModPhys.75.473.
[86] A. Bostwick, T. Ohta, J.L. McChesney, K.V. Emtsev, T. Seyller, K. Horn, E. Rotenberg, Symmetry breaking in few layer graphene films, New J. Phys. 9 (2007) 385, https://doi.org/10.1088/1367-2630/9/10/385.
[87] E.L. Shirley, L.J. Terminello, A. Santoni, F.J. Himpsel, Brillouin-zone-selection effects in graphite photoelectron angular distributions, Phys. Rev. B. 51 (1995) 13614–13622, https://doi.org/10.1103/PhysRevB.51.13614.
[88] D.A. Siegel, C.H. Park, C. Hwang, J. Deslippe, A.V. Fedorov, S.G. Louie, A. Lanzara, Many-body interactions in quasi-freestanding graphene, Proc. Natl. Acad. Sci. U. S. A. 108 (2011) 11365–11369, https://doi.org/10.1073/pnas.1100242108.
[89] C. Hwang, D.A. Siegel, S.K. Mo, W. Regan, A. Ismach, Y. Zhang, A. Zettl, A. Lanzara, Fermi velocity engineering in graphene by substrate modification, Sci. Rep. 2 (2012) 2–5, https://doi.org/10.1038/srep00590.
[90] E. McCann, M. Koshino, The electronic properties of bilayer graphene, Reports Prog. Phys. 76 (2013) 56503, https://doi.org/10.1088/0034-4885/76/5/056503.

[91] T. Taychatanapat, P. Jarillo-Herrero, Electronic transport in dual-gated bilayer graphene at large displacement fields, Phys. Rev. Lett. 105 (2010), 166601, https://doi.org/10.1103/PhysRevLett.105.166601.
[92] K. Kanayama, K. Nagashio, Gap state analysis in electric-field-induced band gap for bilayer graphene, Sci. Rep. 5 (2015) 15789, https://doi.org/10.1038/srep15789.
[93] P. Gava, M. Lazzeri, A.M. Saitta, F. Mauri, Ab initio study of gap opening and screening effects in gated bilayer graphene, Phys. Rev. B. 79 (2009) 1–13, https://doi.org/10.1103/PhysRevB.79.165431.
[94] A. Pradeepkumar, D.K. Gaskill, F. Iacopi, Electronic and transport properties of epitaxial graphene on SiC and 3C-SiC/Si: a review, Appl. Sci. 10 (2020) 1–32, https://doi.org/10.3390/app10124350.
[95] S.M. Choi, S.H. Jhi, Y.W. Son, Effects of strain on electronic properties of graphene, Phys. Rev. B. 81 (2010) 23–26, https://doi.org/10.1103/PhysRevB.81.081407.
[96] C. Klain, S. Linde, R. Shikler, G. Sarusi, Low work function Ca doped graphene as a transparent cathode for organic opto-electronics and OLEDs, Carbon 157 (2020) 255–261, https://doi.org/10.1016/j.carbon.2019.10.028.